Electronic Supplementary Material (ESI) for Journal of Materials Chemistry A.

SUPPORTING INFORMATION

A NiCu-MoS_2 electrocatalyst for pH-universal hydrogen evolution reaction and Zn-air batteries driven self-power water splitting

Mukesh Kumar and Tharamani C. Nagaiah*

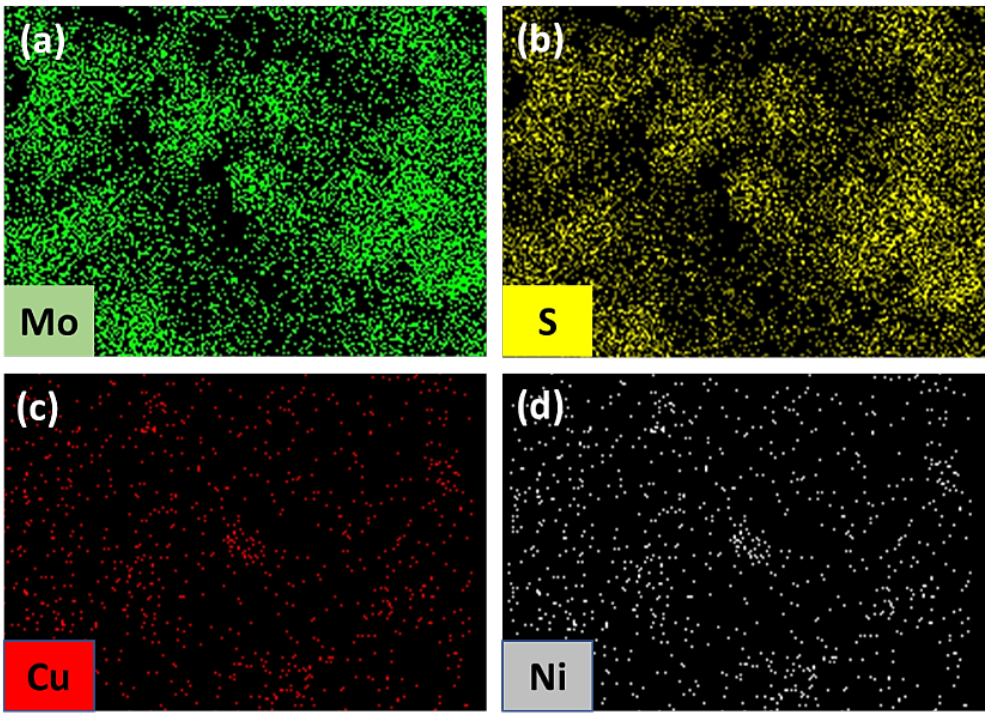

Fig. S1. (a) Elemental dot mapping images representing the distribution of (a) Mo, (b) S, (c) Cu and (d) Ni of NiCu-MoS_2.

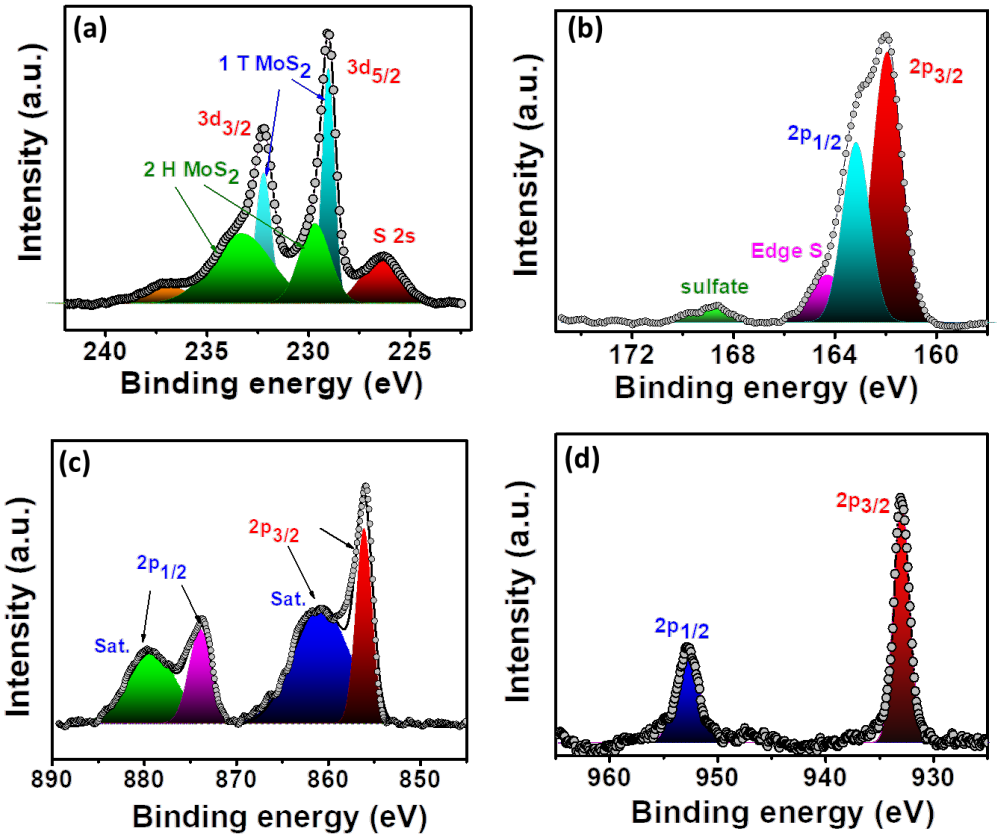

Fig. S2. Deconvoluted XPS spectra of (a) Mo 3d, (b) S 2p, (c) Ni 2p, and (d) Cu 2p of NiCu–MoS_2.

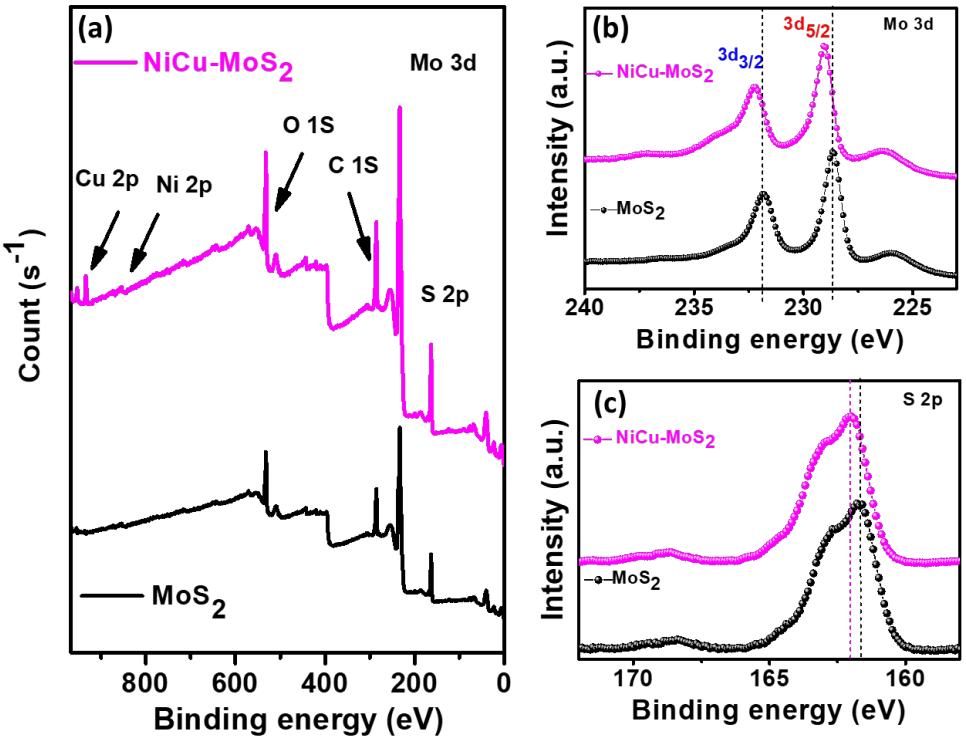

Fig. S3. (a) Comparative XPS survey spectra and XPS spectra of (b) Mo 3d and (c) S 2p of MoS_2 and NiCu–MoS_2.

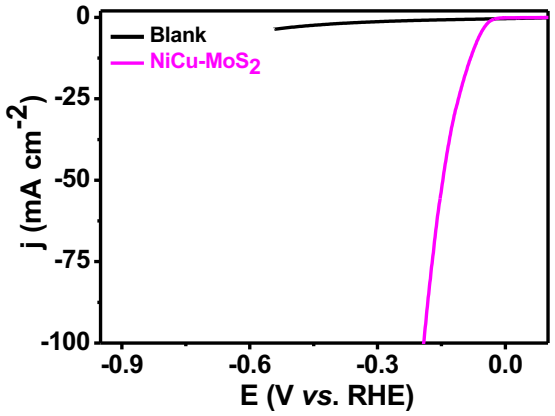

Fig. S4. Linear sweep voltammograms demonstrating HER activity of bare glassy carbon electrode and NiCu-MoS_2 coated glassy carbon electrode in 0.5 M H_2SO_4 electrolyte at a scan rate of 5 mV s^{-1}.

Electrochemical surface area (ECSA):

For the better comparison of the electrocatalytic performance of the various catalysts the determination of the no. of electrochemically active sites is quite beneficial. To determine the no. of electrochemically active sites we have calculated the ECSA. For the ECSA calculation the double-layer capacitance (C_{dl}) was an accepted effective criterion. The ECSA = C_{dl}/C_s (where C_s denoted specific capacitance and was 20-60 μF cm^{-2} in 0.5 M H_2SO_4). In present study the value is selected as 40 μF cm^{-2}. To calculate the double layer capacitance CVs were recorded for the various catalysts in the non-faradaic region from 0.00 to 0.05 V *vs.* RHE at various scan rates ranging from 25-300 mV s^{-1}. The double layer capacitance is calculated by plotting the average current density ($(I_a+I_c)/2$) *vs.* scan rates. [1] After putting these values in above equations the ECSA was obtained. The C_{dl} value obtained for the NiCu-MoS_2 is 376.2 μF, which is divided by 40 μF cm^{-2} to obtained the ECSA. The ECSA shows that the for NiCu-MoS_2 is 9.4 cm^2, higher than all other catalysts showing more active sites are available for the electrochemical reaction.

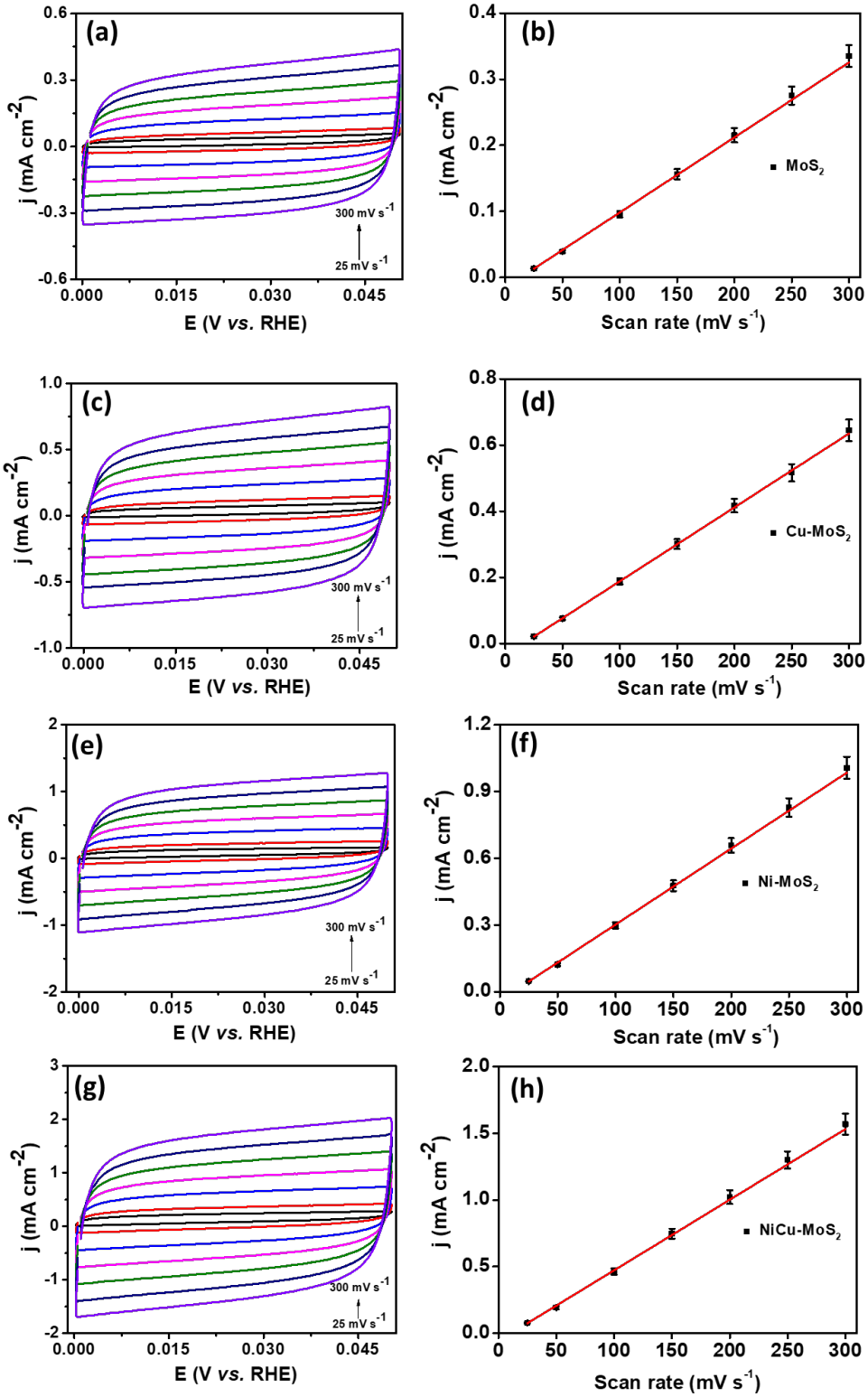

Fig. S5. Cyclic voltammograms of (a) MoS_2, (c) Cu-MoS_2, (e) Ni-MoS_2, (g) NiCu-MoS_2 at various scan rates in the non-faradaic potential region and (b), (d), (f), (h), are corresponding average current versus scan rates plot in 0.5 M H_2SO_4, CE: graphite, RE: Ag/AgCl/3 M KCl.

Table S1: Electrochemical surface area (ECSA determination):

Catalysts	C_{dl} (μF) at 0.025 V *vs.* RHE	ECSA (cm^2)
MoS_2	83.6	2.09
Cu-MoS_2	157.6	3.94
Ni-MoS_2	241.2	6.033
NiCu- MoS_2	376.2	9.4

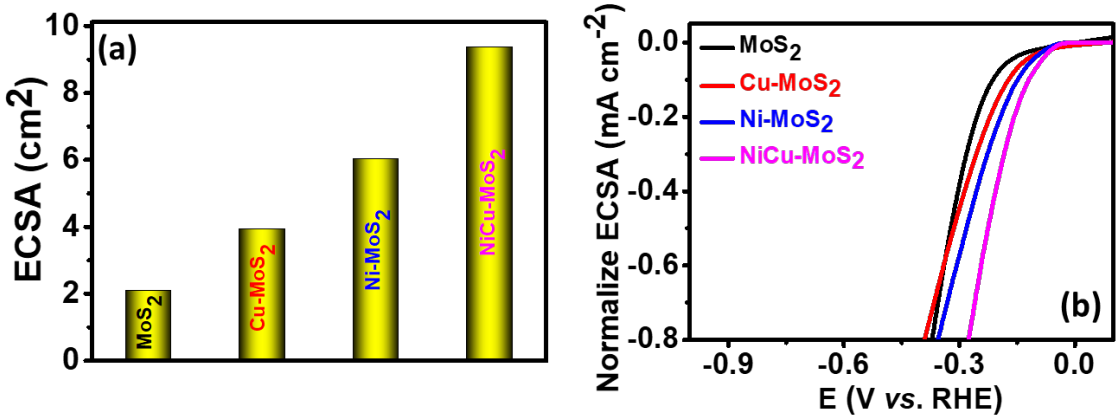

Fig. S6. (a) Bar diagram representing the ECSA of the various catalysts, (b) polarisation curves Normalized with ECSA for various catalysts in 0.5 M H_2SO_4.

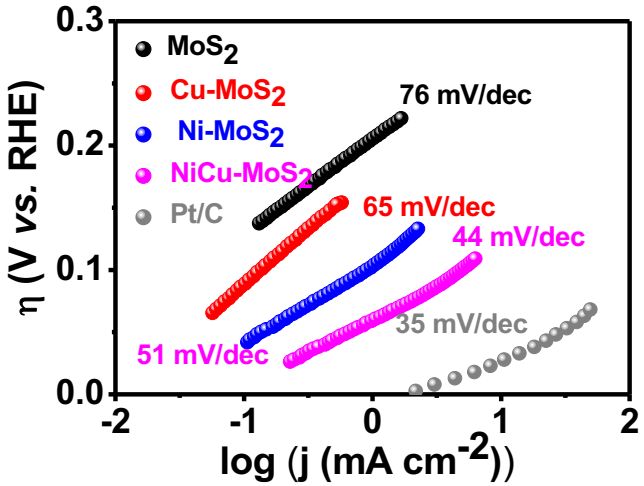

Fig. S7. Tafel plots for various catalysts extracted from Fig. 2a (main manuscript) in 0.5 M H_2SO_4 electrolyte, CE: graphite, RE: Ag/AgCl/3 M KCl.

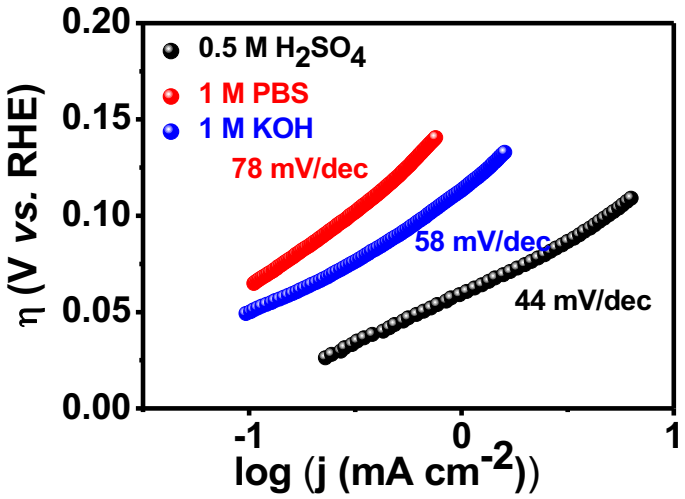

Fig. S8. Tafel plots for NiCu-MoS_2 catalysts in different electrolytes extracted from Fig. 2.

The turnover frequencies (TOFs) for OER and HER were calculated using following equations:

TOF (for HER) = jA/2Fn

TOF (for OER) = jA/4Fn

wherein j is the current density (mA cm^{-2}), A is the area of the electrode (cm^2), n is the no. of moles of the active catalyst; F is the Faraday constant (96 485.3 C mol^{-1}), the number 4 refers to four-electron transfer in the OER process, whereas the number 2 refers to two-electron transfer in the HER process.

Table S2: TOFs of various catalysts for HER @ 150 mV of overpotential in different electrolytes:

Catalysts	0.5 M H_2SO_4	1 M KOH	1 M PBS
MoS_2	0.007	0.0056	0.002
Cu-MoS_2	0.023	0.0153	0.0045
Ni-MoS_2	0.05	0.0375	0.01825
NiCu- MoS_2	0.14	0.16	0.056

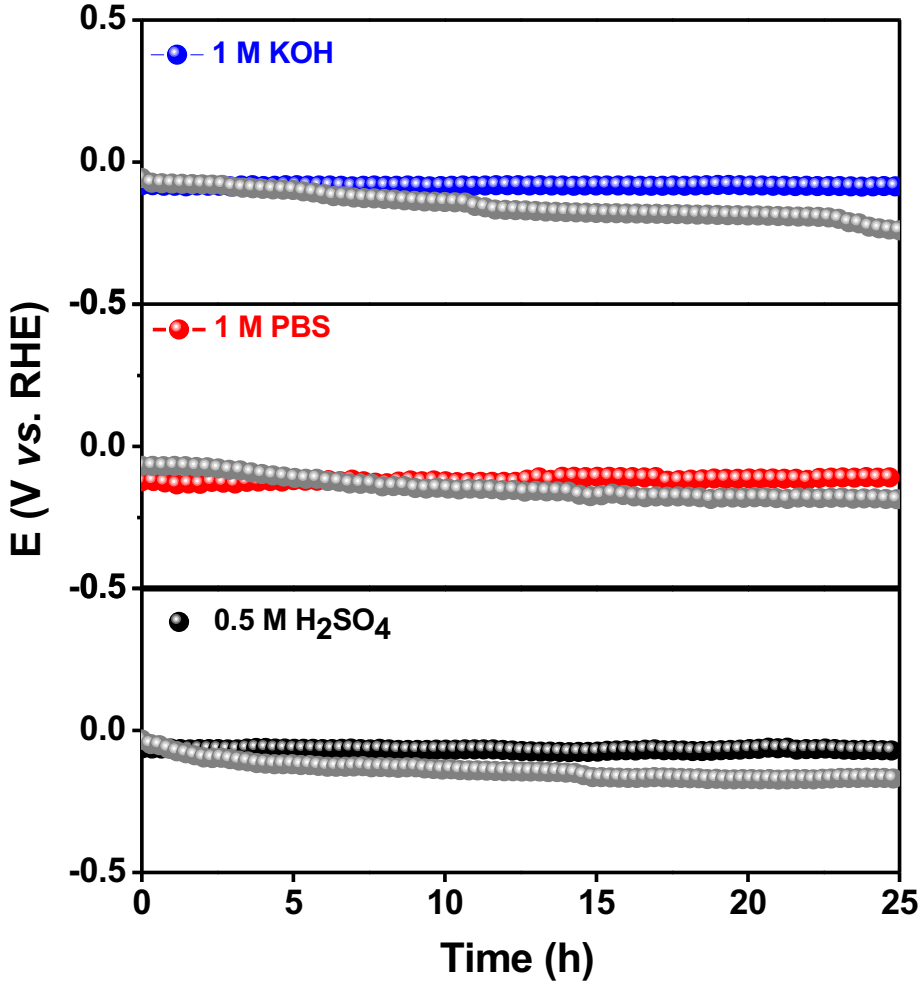

Fig. S9. Chronopotentiometry curve showing cycling stability at -10 mA cm^{-2} for NiCu-MoS_2 and Pt/C in various electrolytes.

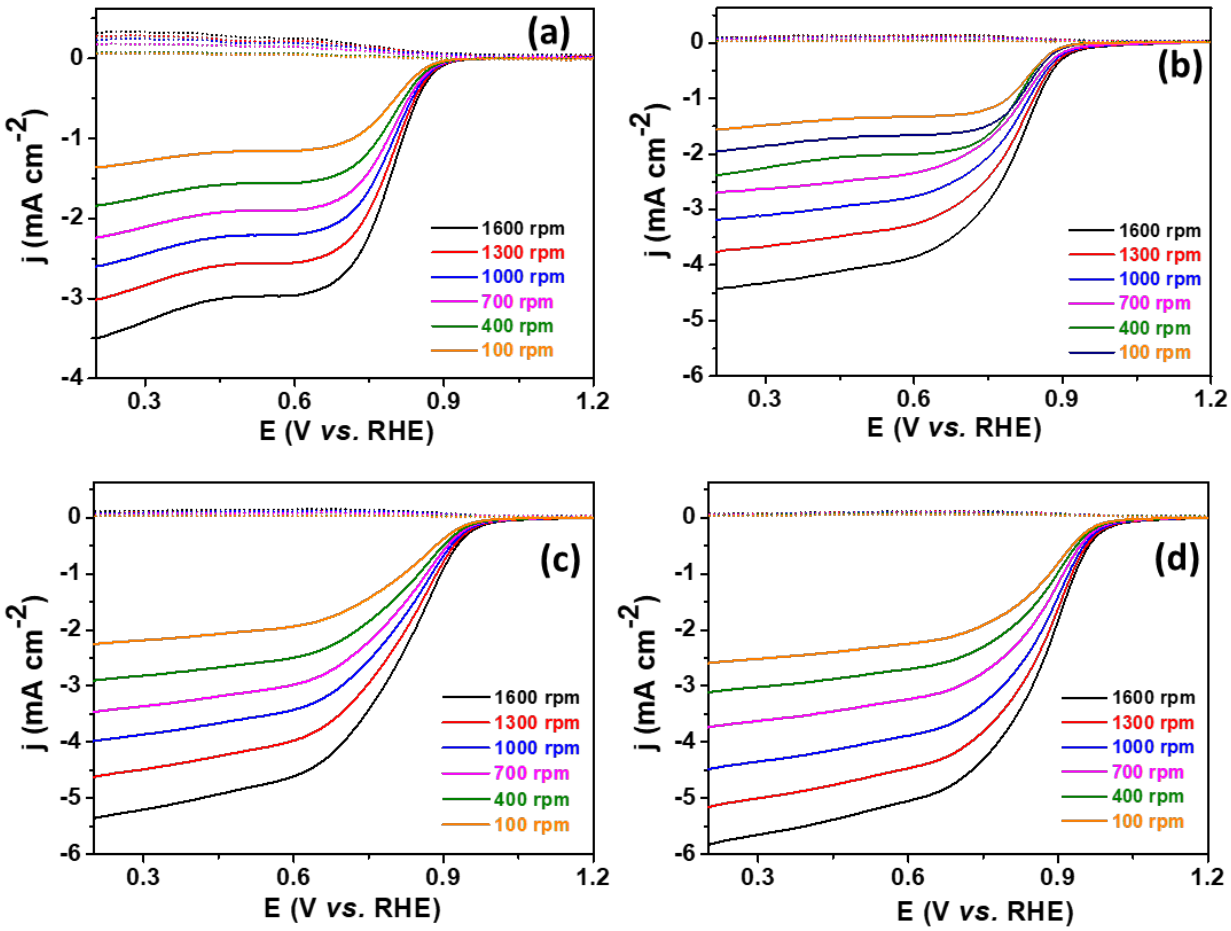

Fig. S10. RRDE Linear polarization curves for (a) MoS_2, (b) Cu-MoS_2, (c) Ni-MoS_2, and (d) NiCu-MoS_2 at varying rotation rates in 0.1 M KOH at a scan rate of 5 mV s^{-1} CE: Pt-wire; RE: Hg/HgO/1 M NaOH.

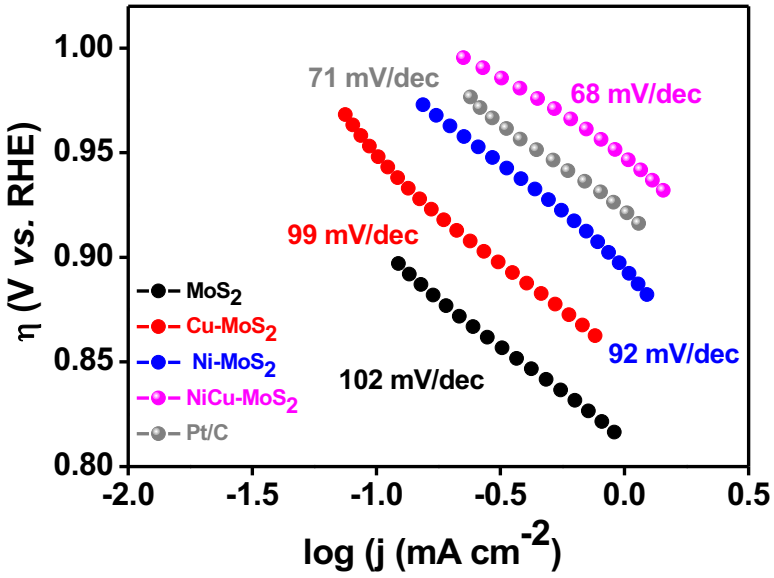

Fig. S11. Tafel plots for various catalysts extracted from Fig. 3b (main manuscript) in 0.1 M KOH electrolyte for ORR, CE: graphite, RE: Hg/HgO/1 M NaOH.

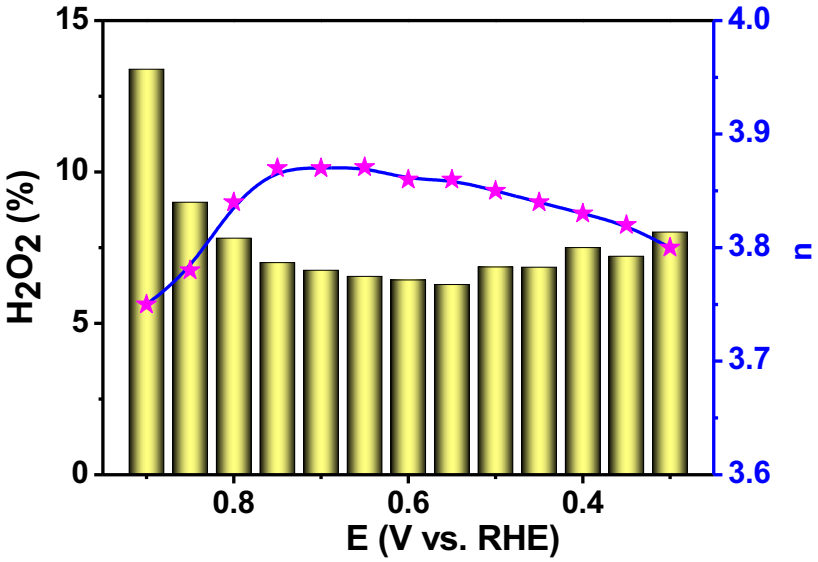

Fig. S12. Bar diagram representing the no. of electron and % of H_2O_2 at various potentials at 1600 rpm.

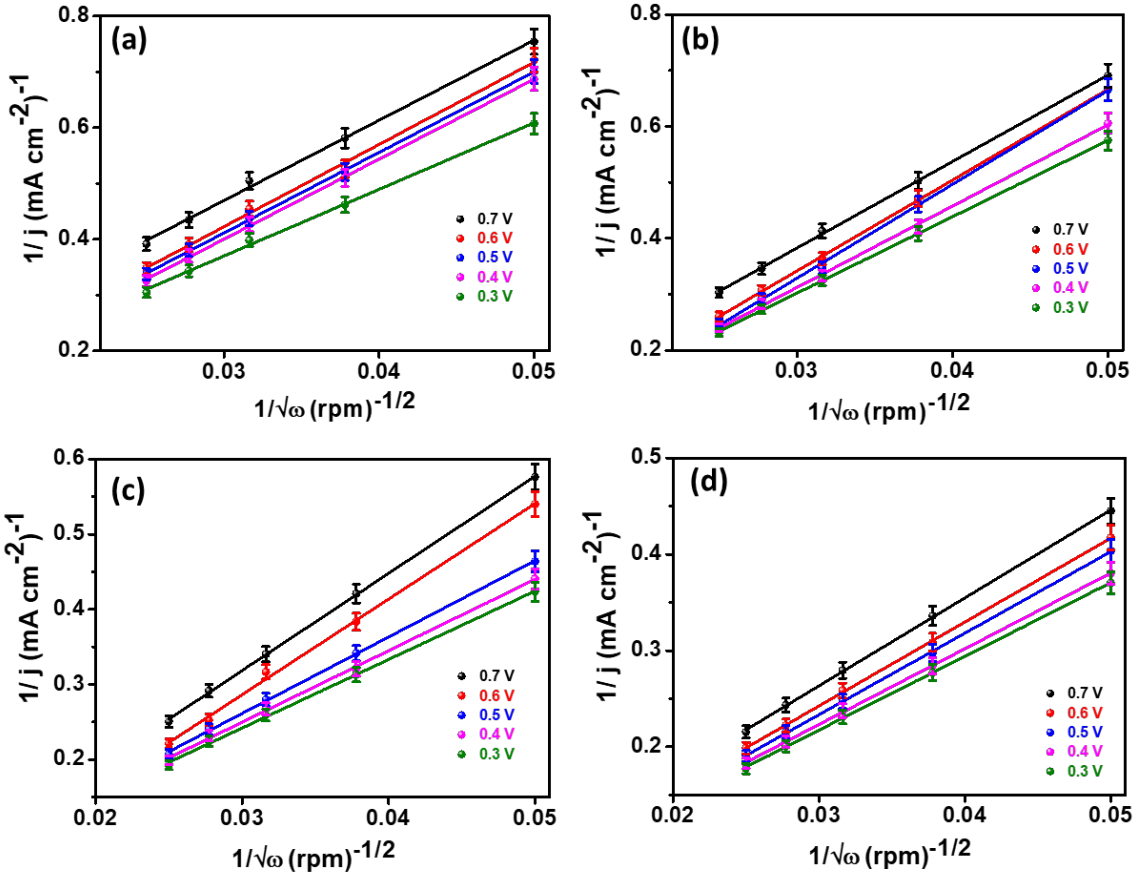

Fig. S13. Koutecky-Levich (K-L) plot for (a) MoS_2, (b) Cu-MoS_2, (c) Ni-MoS_2, and (d) NiCu-MoS_2 at various potential extracted from the linear polarisation curve at various rotation rates in 0.1 M KOH at a scan rate of 5 mV s^{-1}. CE: Pt-wire; RE: Hg/HgO/1 M NaOH.

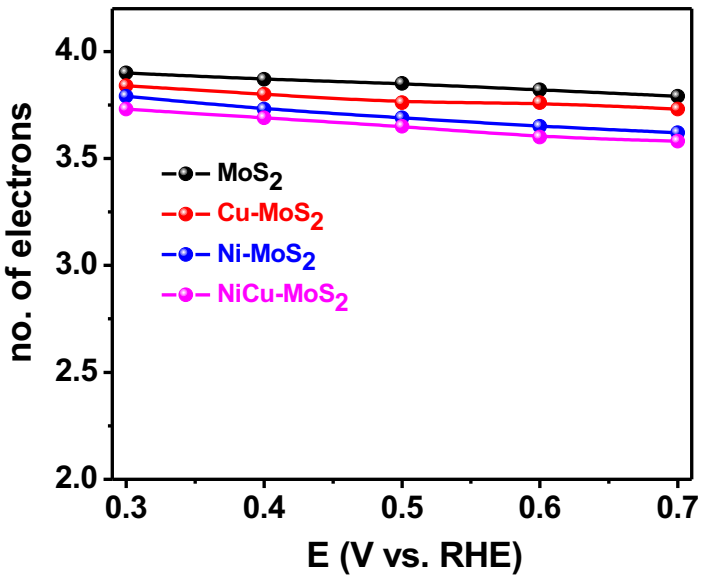

Fig. S14. Potential dependent number of electron extracted from RDE plot in 0.1 M KOH at a scan rate of 5 mV s^{-1}. CE: graphite; RE: Hg/HgO/1 M NaOH.

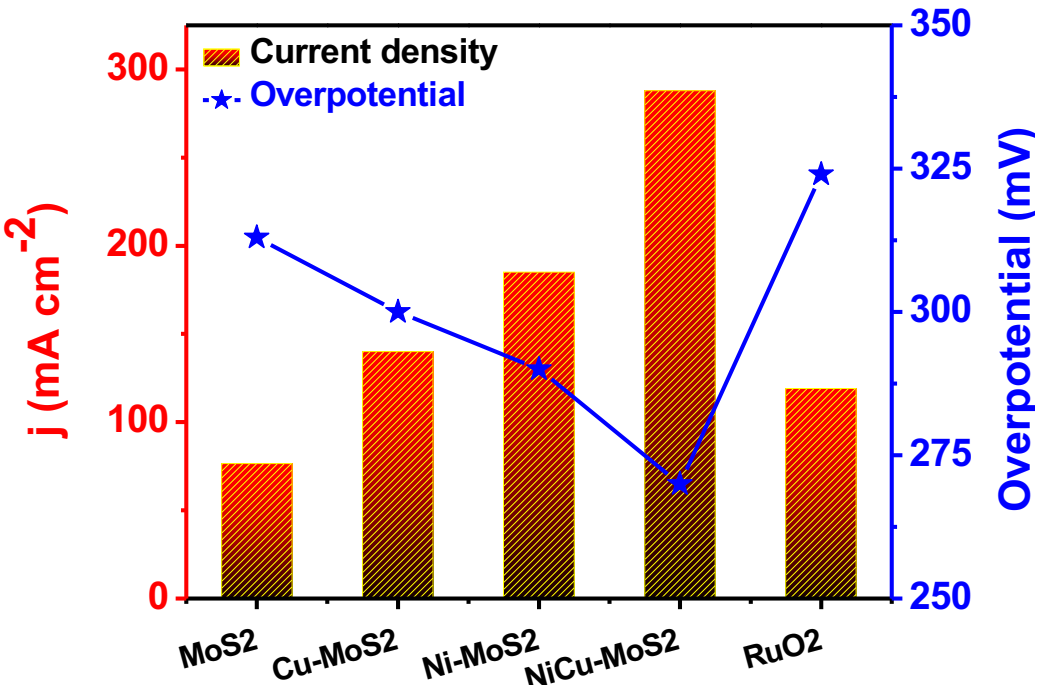

Fig. S15. (a) Bar diagram showing the comparison of obtained current density @ 1.73 V and overpotential @ 10 mA cm^{-2} for various catalysts.

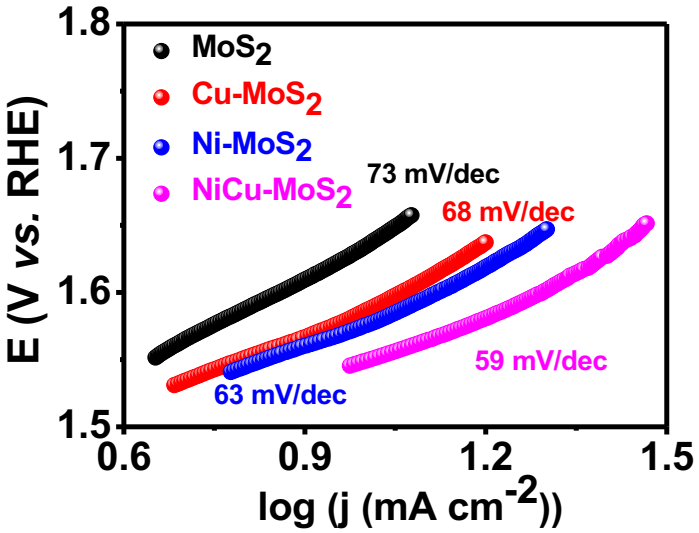

Fig. S16. Tafel plots for various catalysts extracted from Fig. 4a (main manuscript) in 1 M KOH electrolyte for OER, CE: graphite rod, RE: Hg/HgO/1 M NaOH.

Table S3: TOFs of various catalysts for OER @ 1.65 V vs. RHE in 1 M KOH electrolyte:

Catalysts	**1 M KOH**
MoS_2	0.05
Cu-MoS_2	0.093
Ni-MoS_2	0.121
NiCu- MoS_2	0.21

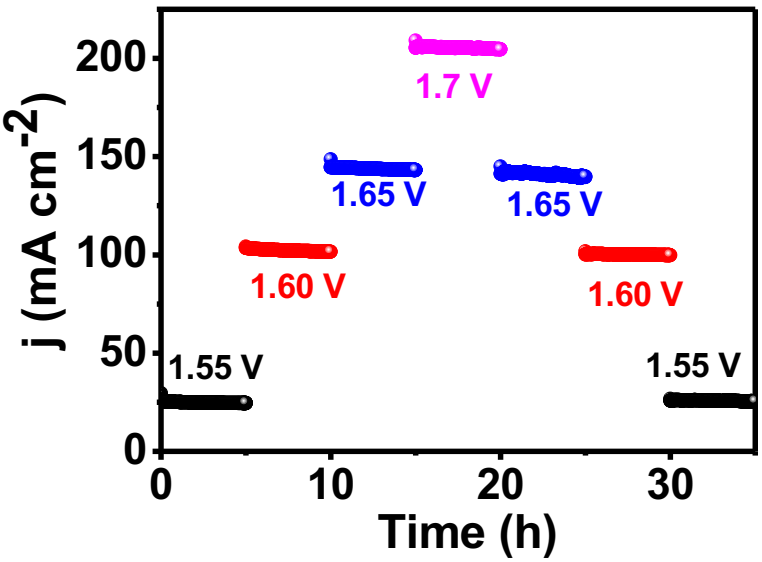

Fig. S17. The multistep chronoamperometric curve for OER by sweeping the potential from 1.55 V to 1.7 V.

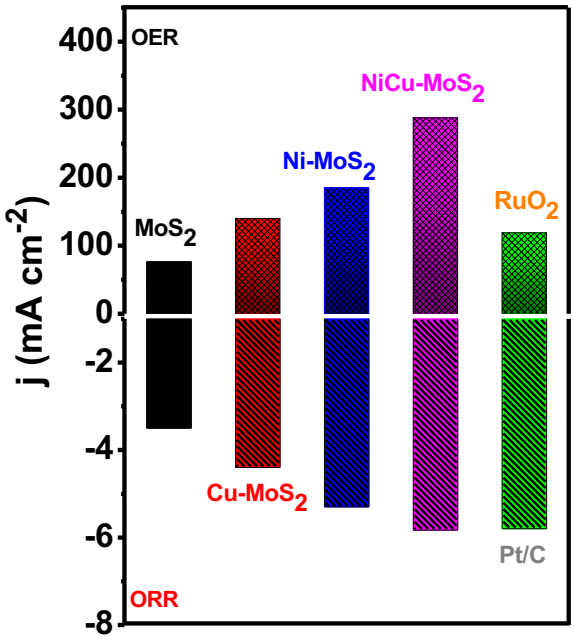

Fig. S18. Bar diagram representing the highest current density of the OER and diffusion limited current density of the ORR.

Fig. S19. Photographic image of the OCV recorded for the battery assembled with NiCu-MoS_2 air cathode.

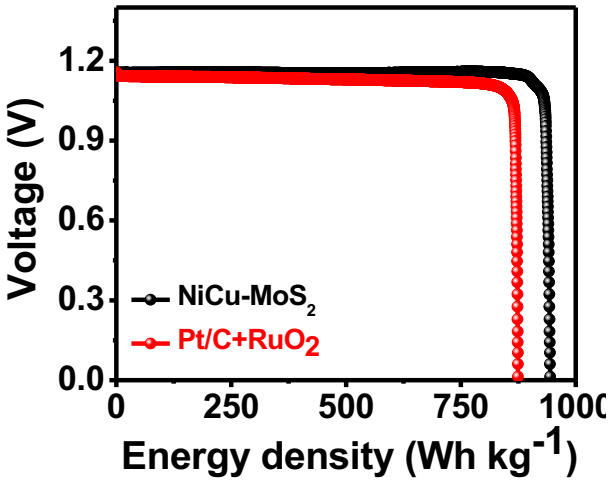

Fig. S20. Energy density of the Zn-air battery assembled with NiCu-MoS_2 and Pt/C+RuO_2 air cathode.

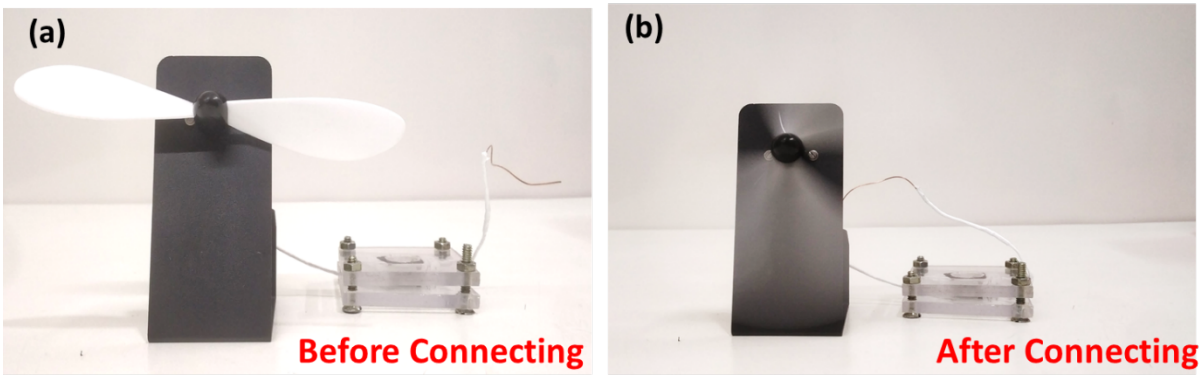

Fig. S21. Photographic images of the fan powered by a single Zn air battery assembled with NiCu-MoS_2 based air cathode.

Round trip efficiency (%) = Discharge voltage/ Charge voltage

For the first cycle,

Round trip efficiency (%) = Discharge voltage/ Charge voltage

= 1.16/1.84

= 63 %

For the 400th cycle,

Round trip efficiency (%) = 1.127/1.854

= 61 %

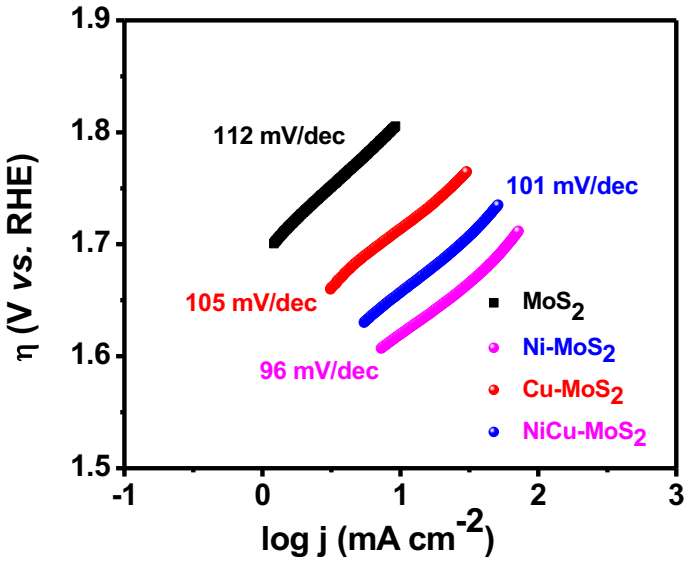

Fig. S22. Tafel plots for various catalysts extracted from Fig. 6a (main manuscript) in 1 M KOH for overall water electrolysis.

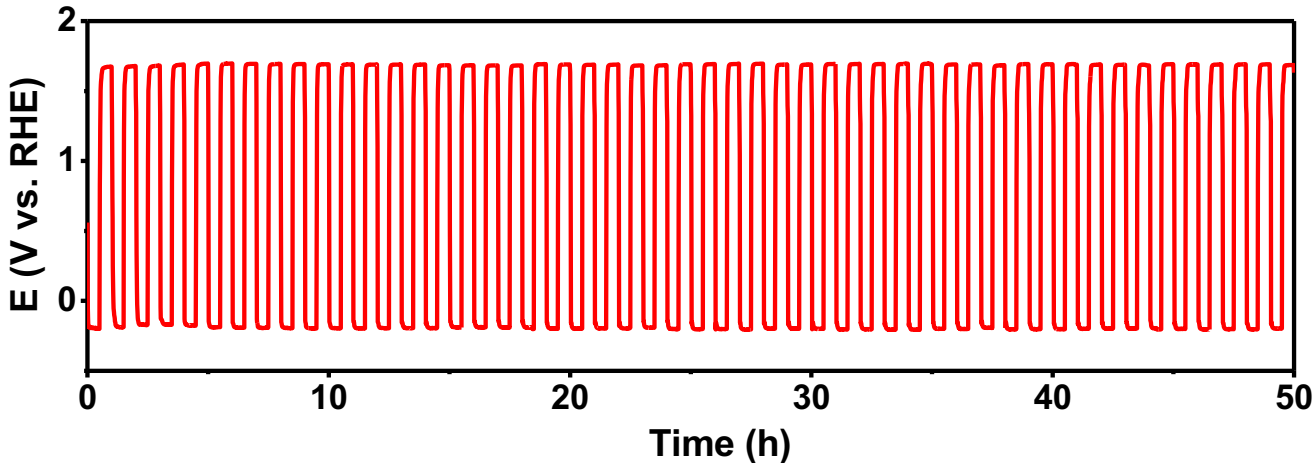

Fig. S23 (a) Chronopotentiometric curve of water splitting device recorded at 100 mA cm^{-2} for OER and -100 cm^{-2} for HER in the three-electrode system where the polarity of a device was reversed after 30 minutes.

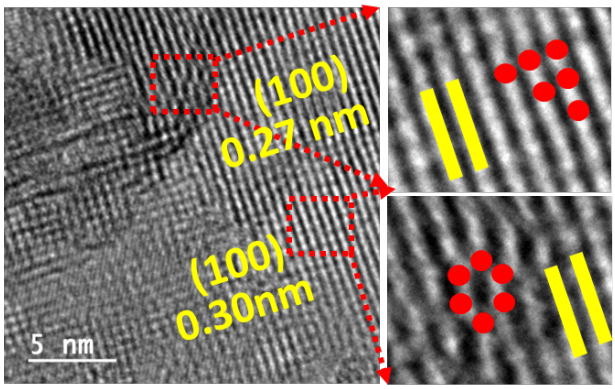

Fig. S24 HR-TEM of NiCu-MoS_2 after HER stability, enlargement shows the 1T phase structure region and its corresponding triangular prismatic structure and 2H phase structure region and its corresponding octahedral structure of NiCu-MoS_2.

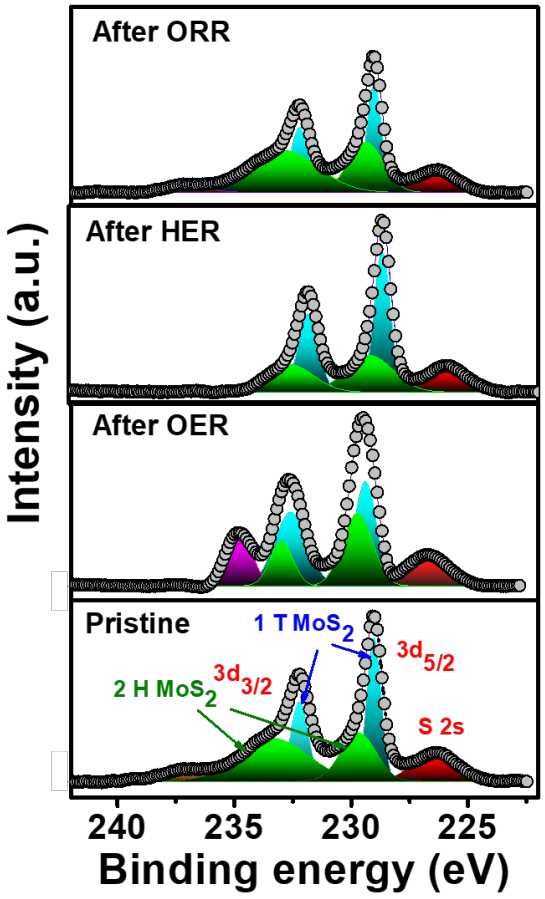

Fig. S25 Deconvoluted XPS spectra of Mo 3d before and after the stability study.

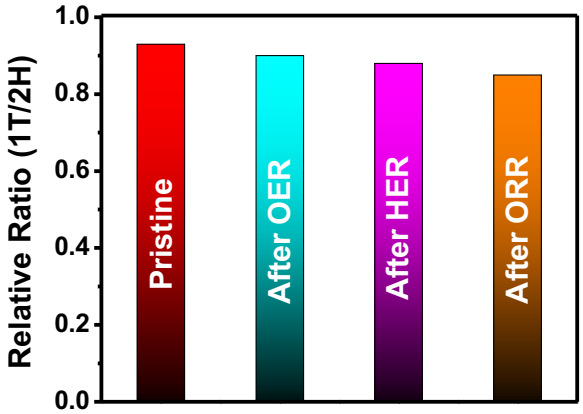

Fig. S26 Relative ratio of 1T/2H phase of NiCu-MoS_2 before and after the stability study.

Table S4: Literature reports showing the self powered water splitting with Zn air batteries:

Catalyst	η@10 mA cm^{-2} in 1.0 M KOH (V)		$E_{1/2}$ ORR (V)	ΔE (V)	ΔE cell (V)	pH universal HER activity	Zn-Air battery		Ref
	OER	HER					Power density (mW cm^{-2})	Specific capacity (mAh g^{-1})	
NiFe/NCNF/CC	0.26		0.79	0.70	2.05	No	141	640	[2]
CoSA + Co_9S_8/ HCNT	0.33	0.25	0.85	0.75	1.59	No	177	788	[3]
CoSA/N,S-HCS	0.31	0.17	0.85	0.67	1.64	No	173	781	[4]
NiS_2 /CoS_2–O NWs	0.24	0.18	0.70		1.77	No			[5]
CoN_x/NGA	0.3	198	0.83	0.70	1.71	No		638	[6]
CoO_x@NOC	0.32	0.25	0.86	0.69	1.51	No	141.65	757	[7]
RuCo/NPC	0.35	0.21	0.80	0.79	1.68	No	79.4	1089	[8]
CoFe@NO –CNT	0.16	0.13	0.84	0.73	1.57	No	142	819	[9]
N, Co-CNTs	0.30	0.20	0.85		1.69	No	114		[10]
CoP@PNC-Do	0.32	0.17 (I M KOH) 0.16 (0.5M H_2SO_4)	0.80		1.74		138	730	[11]
$Ni_{1.9}FeS_{1.09}(OH)_{4.6}$	0.20	0.28@ 80 mA cm^{-2}			1.62	No	248		[12]
Pt/NBF-ReS_2/Mo_2CTx	0.334 (0.1 M KOH)	0.037 1 M KOH 0.049 1 M PBS 0.029 0.5 M H_2SO_4	0.911	0.653		**yes**	180.2	786	[13]
Cu-N-SC-1100	0.33	0.17	0.89	0.67	1.68	No	198	732	[14]
C_{60}-SWCNT	0.46	**0.38 (0.1 KOH) 0.33(PBS) 0.32 (0.5 M H_2SO_4)**	0.79	0.77	1.68	**yes**	NA	NA	[15]
$CoFe(3:1)S_2$	0.25	0.117 1 M KOH 0.12	0.87	0.61	1.58	Yes	387	841	[16]

		1 M PBS 0.98 0.5 M H_2SO_4							
NiCu-MoS_2	**0.290**	**0.081** **1 M KOH** **0.088** **1 M PBS** **0.076** **0.5 M** **H_2SO_4**	**0.856**	**0.66**	**1.622**	**Yes**	**283**	**813**	**This Work**

References:

1. N. Thakur, M. Kumar, S. D. Adhikary, D. Mandal and T. C. Nagaiah, *Chem. Commun.*, 2019, **55**, 5021-5024.
2. C. Lai, J. Fang, X. Liu, M. Gong, T. Zhao, T. Shen, K. Wang, K. Jiang and D. Wang, *Appl. Catal. B: Environ.*, 2021, **285**, 119856.
3. Y. Li, R. Cao, L. Li, X. Tang, T. Chu, B. Huang, K. Yuan and Y. Chen, *Small*, 2020, **16**, 1906735.
4. Z. Zhang, X. Zhao, S. Xi, L. Zhang, Z. Chen, Z. Zeng, M. Huang, H. Yang, B. Liu and S. J. Pennycook, *Adv. Energy Mater.*, 2020, **10**, 2002896.
5. J. Yin, Y. Li, F. Lv, M. Lu, K. Sun, W. Wang, L. Wang, F. Cheng, Y. Li and P. Xi, *Adv. Mat.*, 2017, **29**, 1704681.
6. H. Zou, G. Li, L. Duan, Z. Kou and J. Wang, *Appl. Catal. B: Environ.*, 2019, **259**, 118100.
7. M. E. Hilal, H. A. Younus, S. Chaemchuen, S. Dekyvere, X. Zen, D. He, J. Park, T. Han and F. Verpoort, *Catal. Sci. Technol.*, 2021.
8. Y. Pei, W. He, M. Wang, J. Wang, T. Sun, L. Hu, J. Zhu, Y. Tan and J. Wang, *Chem. Commun.*, 2021, **57**, 1498-1501.
9. M. Li, S. Chen, B. Li, Y. Huang, X. Lv, P. Sun, L. Fang and X. Sun, *Electrochim. Acta*, 2021, **388**, 138587.
10. Q. Jin, B. Ren, H. Cui and C. Wang, *Appl. Catal. B: Environ.*, 2021, **283**, 119643.
11. Y. Li, Y. Liu, Q. Qian, G. Wang and G. Zhang, *Energy Storage Mater.*, 2020, **28**, 27-36.
12. B. Wang, C. Tang, H. F. Wang, B. Q. Li, X. Cui and Q. Zhang, *Small Methods*, 2018, **2**, 1800055.
13. M. Yi, N. Li, B. Lu, L. Li, Z. Zhu and J. Zhang, *Energy Storage Mater.*, 2021, **42**, 418-429.
14. M. Wang, K. Su, M. Zhang, X. Du and Z. Li, *ACS Sustain. Chem. Eng.*, 2021.
15. R. Gao, Q. Dai, F. Du, D. Yan and L. J. J. o. t. A. C. S. Dai, 2019, **141**, 11658-11666.
16. M. Kumar and T. C. Nagaiah, *J.Mater. Chem. A*, 2022, **10**, 4720-4730.